Journal of Materials Chemistry C

ROYAL SOCIETY OF CHEMISTRY

PAPER

View Article Online
View Journal | View Issue

Cite this: J. Mater. Chem. C, 2021, 9, 7632

An ultrafast-response and high-detectivity self-powered perovskite photodetector based on a triazine-derived star-shaped small molecule as a dopant-free hole transporting layer†

Chengwei Shan,‡[a] Fei Meng,‡[a] Jiahao Yu,[a] Zhangxia Wang,[c] Wenhui Li,[a] Dongyu Fan,[a] Rui Chen,[a] Haibo Ma,[c] Gongqiang Li*[b] and Aung Ko Ko Kyaw*[a]

Received 23rd March 2021,
Accepted 13th May 2021

DOI: 10.1039/d1tc01323h

rsc.li/materials-c

Organic–inorganic hybrid perovskites (OIHPs) are becoming appealing for photodetectors due to their excellent optoelectronic properties, but the drawbacks of the commonly used interfacial layers in OIHP photodetectors such as the necessity of doping, high cost and stability issues hinder the further development of this technology. Herein, a star-shaped small molecule with a triazine core unit named Triazine-Th-OMeTAD was synthesized and employed as a dopant-free hole transporting layer in an OIHP photodetector. The Triazine-Th-OMeTAD provided a low-trap-density perovskite film, efficient charge extraction and a large electron injection barrier. As a result, the optimized OIHP photodetector with the Triazine-Th-OMeTAD HTL exhibited a low dark current of 1.09 nA cm^{-2}, a high responsivity of 0.47 A W^{-1}, and a high specific detectivity of over 8.2 × 10^{12} Jones at zero bias. Remarkably, a response speed of 18 ns was obtained at a large active area of 11 mm^2. The high-performance OIHP photodetector demonstrated here acts as a promising candidate for low-cost and high-performance near-ultraviolet-visible photodetection, which is applicable in quick frame rate visible imagers, optical communications and many more.

Introduction

Photodetectors, which convert incident photons into free charge carriers, are extremely important to industrial and scientific applications, including optical communications, environmental monitoring, biological sensing and surveillance camera systems.[1–4] Therefore, photodetectors with self-power detection, broad spectrum detection, fast response, high responsibility (R) and high detectivity (D^*) have high commercialization prospects. Recently, organic–inorganic hybrid perovskites (OIHPs) have attracted extensive attention for photodetectors due to their solution-processibility as well as their excellent intrinsic optoelectronic properties such as non-excitonic features,[5] direct bandgaps with large absorption coefficients in the UV-vis range,[6] long carrier diffusion lengths, high mobility with balanced charge transport,[7] and low defect densities.[8] Because of high absorption coefficients, OIHP-based photodetectors can be made with a very thin active layer (a few hundred nanometers only), which can further reduce the transit time of carriers, demonstrating good potential for fast-response photodetectors in a sub-nanosecond time scale.[9] A good response only in the UV-vis region yet negligible response in the NIR region is also attractive for imagers in digital cameras, eliminating the necessity of infrared filters for high image quality.[9] A remarkable device performance was achieved by manipulating the perovskite film with various techniques such as cation engineering,[10] gradient 3D/2D perovskite films for efficient charge separation,[11] thin single-crystal films[12] and so on.

In addition to high-quality OIHP crystals, interface engineering with electron transport layers (ETLs) or hole transport layers (HTLs) is also critical for achieving high-performance OIHP photodetectors. With interface engineering, charge recombination and dark current are suppressed *via* surface trap passivation,[9,13] increasing carrier injection barriers,[14] and efficient charge carrier extraction at the interfaces,[15] while the device stability is also

[a] Guangdong University Key Laboratory for Advanced Quantum Dot Displays and Lighting, Department of Electrical & Electronic Engineering, Southern University of Science and Technology, Shenzhen 518055, P. R. China.
E-mail: aung@sustech.edu.cn
[b] Institute of Advanced Materials (IAM), Nanjing Tech University (NanjingTech), 30 South Puzhu Road, Nanjing 211816, P. R. China.
E-mail: iamgqli@njtech.edu.cn
[c] School of Chemistry and Chemical Engineering, Nanjing University, Nanjing 210023, P. R. China

† Electronic supplementary information (ESI) available. See DOI: 10.1039/d1tc01323h

‡ These authors contributed equally.

improved *via* the encapsulation effect.[16] The efficient charge extraction and dark current reduction eventually lead to large responsivity, high specific detectivity, and fast response time for further improvement in the performance of perovskite photodetectors.[17,18] However, there are several drawbacks in the commonly used HTLs of the reported OIHP photodetectors, for both regular and inverted structures. For example, Spiro-OMeTAD, a state-of-the-art HTL used in regular structure devices, requires ionic salt doping to improve the hole conductivity, and in turn to accelerate the response time of the photodetector, but doping adversely affects the stability of the device.[19] Moreover, it requires multistep synthesis, which makes the material expensive (roughly 400 USD per gram),[20] resulting in high production cost for commercial photodetectors. On the other hand, poly(3,4-ethylenedioxythiophene)poly(styrenesulfonate) (PEDOT:PSS) is a commonly used HTL in inverted structure devices. Unlike Spiro-OMeTAD, it does not require any doping but its hygroscopic and acidic nature leads to the degradation of the perovskite film and corrosion of the electrodes and hence, negatively influences the stability of the device.[21,22] Besides, another key issue associated with PEDOT:PSS is that the grain size of the perovskite crystals fabricated on PEDOT:PSS is relatively small thanks to the hydrophilic nature of PEDOT:PSS, resulting in recombination loss at grain boundaries and relatively slow response time of the device.[17,23] Compared with PEDOT:PSS, the hydrophobic poly[bis(4-phenyl)(2,4,6-trimethyphenyl)amine] (PTAA) plays an important role in the growth of grains and the reduction of the grain boundary area, and it also minimizes the grain boundary energy.[9,24] Therefore, the photodetector with PTAA as the HTL exhibited a fast response time of $\sim$1 ns for a small active area of 0.04 mm^2, but the response is still slow for a large active area (115.1 ns for an active area of 7 mm^2)[9] and hence, it is not appealing for large-area photodiodes, which is usually ideal for instrumentation and monitoring applications. Moreover, PTAA is extremely expensive, and its cost is about 50 times that of gold, hindering its application in large-scale manufacturing. Therefore, it is extremely urgent to explore new HTMs to further improve the device performance of OIHP photodetectors without comprising the stability and cost, but only a few new HTMs have been reported for OIHP photodetectors so far.[17]

Recently, our group has developed a couple of new small molecules as dopant-free HTLs for OIHP solar cells by employing a cyclooctatetrathiophene (COTh) or bifluorenylidene core with a triphenylamine arm unit.[25–27] These easy and costless synthesized dopant-free HTLs demonstrate excellent advantages on charge extraction and transfer, crystallization and passivation of OIHP, yielding high power conversion efficiency and very good stability. All these results inspired us to explore their applications in OIHP photodetectors. Herein, we synthesized a new hole transporting material with a star-shaped donor–π–acceptor (D–π–A) system named Triazine-Th-OMeTAD[28] by employing an electron-deficient 1,3,5-triazine as the core, thiophene as the π-linker and the triphenylamine unit as the ending group in only one-step with low cost and high total yields. Considering the chemical structure, the new HTM may have several advantages in OIHP photodetector devices, such as: (1) with the planar 1,3,5-triazine core and thienyl units, Triazine-Th-OMeTAD will display much better intermolecular π–π stacking interactions and yield higher hole mobility compared to spiro-orthogonal structures,[22] which is beneficial to efficient charge extraction and transfer, and in turn, fast response speed;[28] (2) the *N*-enriched triazine and thienyl units can enhance the interactions of HTLs with both ITO and the perovskite layer, which will boost the hole transport from the perovskite to the electrode; and (3) as a sub-layer in inverted structures, N, S, and O will also enhance the crystallinity and passivation of OIHP, resulting in larger grain size, better film coverage and higher crystallinity of OIHP films.[29] All these advantages promise us an excellent perspective of Triazine-Th-OMeTAD in OIHP photodetectors.

We first utilized Triazine-Th-OMeTAD as the dopant-free HTL in an inverted planar structure perovskite ($MAPbI_3$) photodetector and demonstrated an unprecedented device performance. As promised, it also serves as a foundation layer for the growth of high-quality $MAPbI_3$ crystalline films with large grain sizes. Moreover, a very shallow LUMO level of Triazine-Th-OMeTAD creates a huge electron injection barrier, which is an important criterion for a high-performance photodetector to reduce dark current. In addition, it provides efficient hole extraction from perovskite due to the suitable energy-level alignment with the perovskite and high hole mobility, leading to fast response speed in the photodetector. Through optimizing the thickness of Triazine-Th-OMeTAD (concentration of precursor solution), the OIHP photodetectors achieve a low dark current density of 1.09 nA cm^{-2}, a responsivity (R) of 0.47 A W^{-1}, a very fast response speed of 18 ns for a large active area (11 mm^2), a large dynamic linear response range of 166 dB and a specific detectivity exceeding 8.2×10^{12} Jones at zero bias. Our result indicates that with appropriate HTLs, the OIHP photodetectors act as a promising candidate for high-performance self-powered UV-visible photodetection.

Results and discussion

The compound of Triazine-Th-OMeTAD (Fig. 1) was synthesized by the Suzuki cross-coupling reaction as shown in the Scheme (Fig. S1, ESI†). The detailed synthesis route of Triazine-Th-OMeTAD can be found in the ESI.† To understand the electronic structure of Triazine-Th-OMeTAD, theoretical calculations based on density functional theory (DFT) were performed using the Gaussian 09 software package.[30] The monomer geometry was optimized at the PBE0/6-31G(d,p) level,[31] and the frequency check was used to ensure the nature of the stationary point for the optimized molecule. As shown in Fig. 1a, the 1,3,5-triazine and thienyl units are in the same plane and the degree of distortions between the thienyl units and the triphenylamine units is 21.2°, 21.0° and 21.2°, respectively. (θ_1, θ_2, and θ_3 in Fig. 1a).

The frontier molecular orbitals (FMOs) were employed to illustrate the carrier transport capability. The spatial distribution of the highest occupied molecular orbital (HOMO) and the lowest unoccupied molecular orbital (LUMO) is plotted in

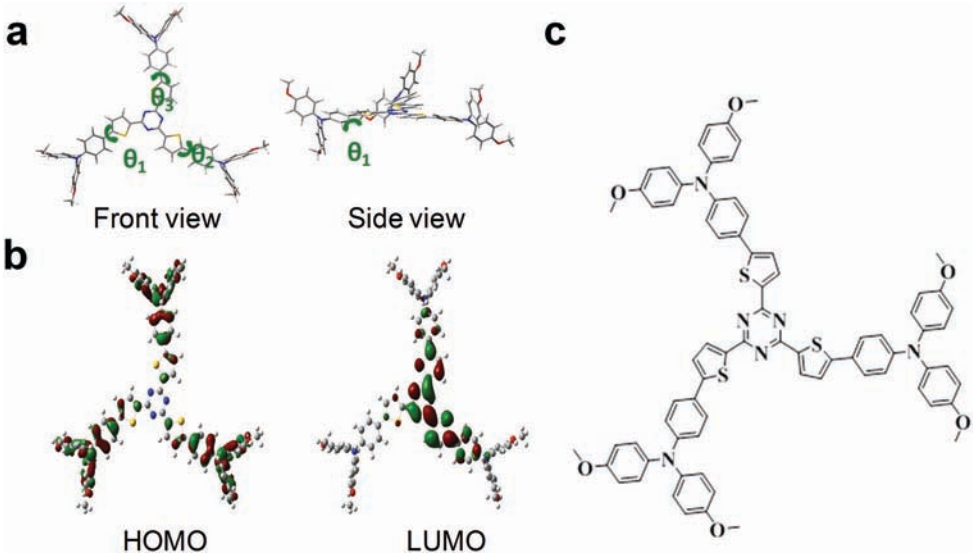

Fig. 1 (a) Optimized geometry of Triazine-Th-OMeTAD; (b) FMO distributions of Triazine-Th-OMeTAD at the PBE0/6-31G(d,p) level; and (c) the chemical structure of Triazine-Th-OMeTAD.

Fig. 1b. The electron density flows from the end groups to the core groups for the HOMO → LUMO excitations. The distributions of HOMO and LUMO spread over the conjugated backbone show π-orbital features. The HOMO is mainly localized on the triphenylamine units and the thienyl units, while the LUMO is mainly distributed on the 1,3,5-triazine core and the thienyl moieties with negligible contributions from the triphenylamine units. This demonstrates that the triphenylamine units serve as donors while the thienyl units and 1,3,5-triazine core serve as acceptors, respectively. Additionally, the calculated E_{HOMO} and E_{LUMO} values (−5.00 eV and −2.49 eV, $E_{LUMO} = E_{HOMO} + E^{ex}$, where E^{ex} represents the first vertical excited energy[32–34]) at the PBE0/6-31G(d,p) level are close to the experimental results.

Based on the optimized structure, the absorption spectra of Triazine-Th-OMeTAD in both the solution and the film state were studied by UV-vis measurements. As shown in Fig. S5 (ESI†) and Table 1, Triazine-Th-OMeTAD exhibits the λ_{abs}/max around 400–550 nm. The absorption bands in the 300–350 nm region can be assigned to the π–π* transition of the triphenylamine moieties.[35] The absorption at 455 nm of Triazine-Th-OMeTAD in solution is attributed to the π–π* transition of the conjugated system of the triphenylamine unit and triazine core. The absorption spectrum of the spin-coated thin film is slightly broadened and red-shifted, in comparison to that of a solution, due to the slightly stronger intermolecular π–π stacking in the film.[36–39] The optical bandgap of Triazine-Th-OMeTAD is estimated to be 2.30 eV based on the absorption onset at 538 nm of the film. The HOMO energy level of Triazine-Th-OMeTAD is −5.57 eV, which is determined by ultraviolet photoelectron spectroscopy (Fig. S6, ESI†), indicating a well-match with the valence band edge of the perovskite. The LUMO is −3.27 eV, which is calculated from the HOMO energy and optical bandgap. All the optical and electrochemical properties are summarized in Table 1.

The thermal behaviour of HTM was determined by thermal gravimetric analysis (TGA) and differential scanning calorimetry (DSC) measurements as shown in Fig. S7 (ESI†) and Table 1. Triazine-Th-OMeTAD displays a good thermal stability in the TGA test with 5% weight loss observed at 449 °C. DSC scans demonstrate that Triazine-Th-OMeTAD is naturally in amorphous phases, with a glass transition temperature (T_g) observed at 140 °C. A high decomposition temperature (T_d = 422 °C) and a glass transition temperature (T_g = 140 °C) are essential for device fabrication and the long-term photostability of photodetectors, particularly in the p–i–n structure, in which the perovskite is deposited on top of the HTM and subsequently thermally annealed at elevated temperatures. The space charge limited current (SCLC) method was used to estimate the hole mobility of Triazine-Th-OMeTAD by constructing a hole-only device with a structure of ITO/PEDOT:PSS/Triazine-Th-OMeTAD/Au. A hole mobility of 2.06×10^{-4} cm^2 V^{-1} s^{-1} was obtained from the SCLC measurements (Fig. S8, ESI†), exhibiting high mobility, which is beneficial for charge transport to the electrode.

Table 1 Optical and electrochemical properties of Triazine-Th-OMeTAD

	λ_{sol}[a] [nm]	λ_{film}[b] [nm]	E_g^{opt}[c] [eV]	E_{HOMO}[d] [eV]	E_{LUMO}[e] [eV]	T_d [°C]	T_g [°C]	μ_h [cm^2 V^{-1} s^{-1}]
Triazine-Th-OMeTAD	455	460	2.30	−5.57	−3.27	449	140	2.06×10^{-4}

[a] Solution absorption spectra (1×10^{-5} M in chloroform). [b] Absorption spectra of films on quartz. [c] Optical bandgap (E_g^{opt}) estimated from the edge of absorption spectra. [d] Determined by ultraviolet photoelectron spectroscopy. [e] $E_{LUMO} = E_{HOMO} + E_g^{opt}$.

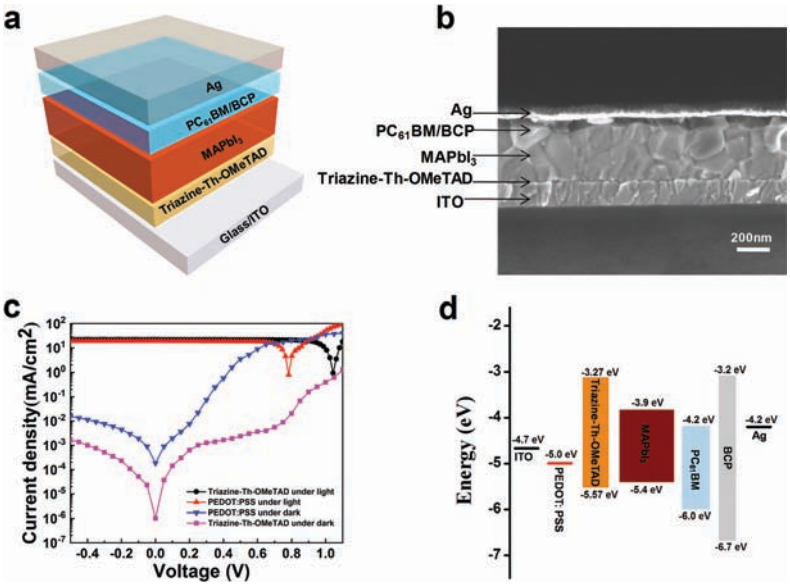

Fig. 2 (a) Schematic device structure; and (b) the cross-sectional SEM image of the OIHP photodetector; (c) current density–voltage (*J*–*V*) characteristics: photocurrent density under air mass 1.5G illumination (100 mW cm^{-2}), and dark current density of the OIHP photodetector; (d) the schematic energy diagram of the OIHP photodetector, comparing the energy levels of Triazine-Th-OMeTAD and PEDOT:PSS.

To investigate the application of Triazine-Th-OMeTAD as an HTL in photodetectors, we fabricated the $MAPbI_3$ perovskite films on top of the Triazine-Th-OMeTAD layer *via* a simple one-step solution process followed by a subsequent thermal annealing step. The device structure of our OIHP photodetectors is schematically shown in Fig. 2a and composed of indium tin oxide (ITO)/Triazine-Th-OMeTAD/$MAPbI_3$/phenyl-C_{61}-butyric-acid methyl ester ($PC_{61}BM$)/2,9-dimethyl-4,7-diphenyl-1,10-phenanthroline (BCP)/silver (Ag). We also prepared the devices with PEDOT:PSS as an HTL, for comparison. The star-shaped Triazine-Th-OMeTAD plays an important role in the formation of high-quality perovskites, which can be clearly seen in the cross-sectional scanning electron microscopy (SEM) image of the perovskite film on Triazine-Th-OMeTAD (Fig. 2b). The perovskite film is very flat, which also indicates that the film is 257 nm thick. After that, it can be seen that the $PC_{61}BM$ (50 nm)/BCP (8 nm) completely covers the whole perovskite layer, avoiding direct contact between the perovskite layer and the cathode metal, hence reducing the leakage current. Finally, the device fabrication was finished by the thermal evaporation of 100 nm silver (Ag) as the top electrode. Fig. 2c displays the dark current and photocurrent density (under air mass 1.5 global illumination) of the OIHP photodetectors under the bias ranging from −0.5 V to 1.0 V. It can be seen that the reverse-bias dark current of the Triazine-Th-OMeTAD-based photodetector exhibits a value of 1.0×10^{-3} mA cm^{-2} under −0.5 V, which is two orders of magnitude smaller than that of the PEDOT:PSS-based photodetector. It can also be seen that the photocurrent of the Triazine-Th-OMeTAD-based device is about 22 mA cm^{-2}, which is higher than that of the PEDOT:PSS-based device, exhibiting a high on–off ratio. This enables OIHP photodetectors to achieve a large linear dynamic range (LDR) and high specific detectivity. The energy levels of individual layers used in the OIHP photodetector are shown in Fig. 2d. Under illumination, the electron–hole pairs are generated in the perovskite, and the holes are extracted by HTL to the ITO electrode while the electrons are extracted *via* PCBM to the Ag electrode, generating the corresponding photocurrent. The LUMO level of Triazine-Th-OMeTAD is −3.27 eV, therefore, with Triazine-Th-OMeTAD as the HTL, the electron injection barrier between ITO and $MAPbI_3$ increases significantly from 0.8 to 1.43 eV. This considerably suppressed the electron injection in the dark from the external circuit and thus reduces the dark current.[9,17,40] A strong dark current suppression by a large electron injection barrier was also observed in organic photodetectors.[41,42] On the other hand, this low dark current can also be attributed to BCP, which can create a large hole injection barrier of 2.5 eV at the Ag/BCP interface.

To further understand how the star-shaped Triazine-Th-OMeTAD enhances the performance of the OIHP photodetector, various characterizations were carried out. We optimized the thickness of Triazine-Th-OMeTAD by varying the concentrations of Triazine-Th-OMeTAD (namely, 0.5 mg mL^{-1}, 1.0 mg mL^{-1}, 2.0 mg mL^{-1}, 3.0 mg mL^{-1} and 6.0 mg mL^{-1} in chlorobenzene). The average thicknesses of the films fabricated from 0.5 mg mL^{-1}, 1.0 mg mL^{-1}, 2.0 mg mL^{-1}, 3.0 mg mL^{-1} and 6.0 mg mL^{-1} concentrations are 5.3 nm, 7.9 nm, 15.8 nm, 21.4 nm and 31.7 nm, respectively (Fig. S9, ESI†). The atomic force microscopy (AFM) was then performed to examine the surface topography of the Triazine-Th-OMeTAD films fabricated from different concentrations and the PEDOT:PSS film. As shown in Fig. S10 (ESI†), this star-shaped material exhibits a smoother and more homogeneous surface with a root-mean-square (rms) roughness of 1.424 nm, compared to PEDOT:PSS with an rms of 1.913 nm. In an inverted structure photodiode, the HTL also serves as a foundation layer for the perovskite crystal growth, and hence influences the morphology of the

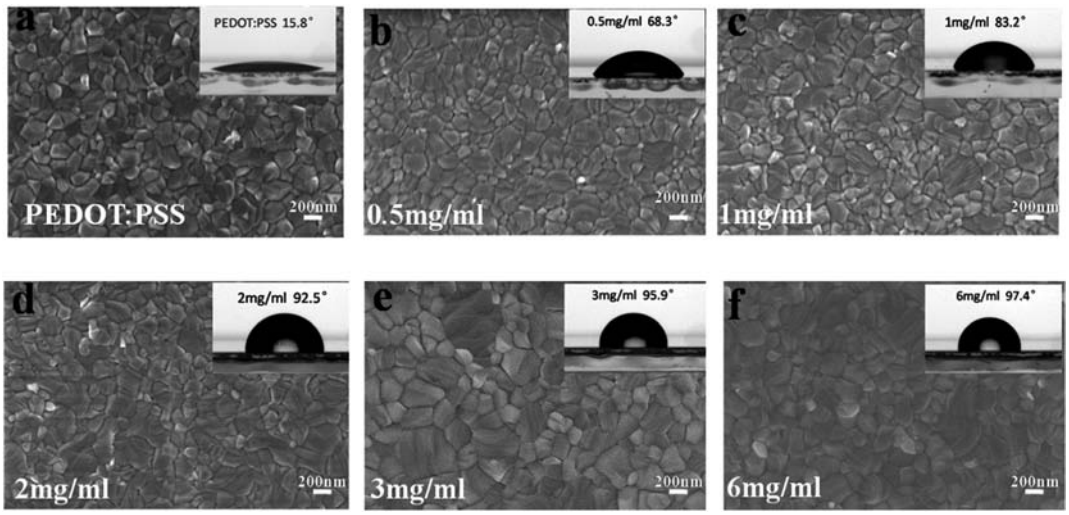

Fig. 3 Surface SEM images of the $MAPbI_3$ layer on (a) PEDOT:PSS; (b) 0.5 mg mL^{-1} Triazine-Th-OMeTAD; (c) 1.0 mg mL^{-1} Triazine-Th-OMeTAD; (d) 2.0 mg mL^{-1} Triazine-Th-OMeTAD; (e) 3 mg mL^{-1} Triazine-Th-OMeTAD and (f) 6.0 mg mL^{-1} Triazine-Th-OMeTAD, and the insets are the contact angels of the deionized water on the surface of different HTLs.

perovskite film. Therefore, the morphology of perovskite films fabricated on different concentrations of Triazine-Th-OMeTAD as well as on PEDOT:PSS was examined. As shown in Fig. 3a–f, the grain size of perovskite is small on PEDOT:PSS, while it becomes larger on Triazine-Th-OMeTAD. It has been reported that the hydrophobicity and dense surface can lead to a large perovskite crystal size, but PEDOT:PSS is classified as a hydrophilic surface.[24] Herein, we discuss the role of different HTLs on perovskite crystallization more directly by the contact angle measurements of the deionized water, which is displayed in the insets of Fig. 3a–f. It can be found that the deionized water has a much stronger surface affinity for PEDOT:PSS than Triazine-Th-OMeTAD. There is a strong interfacial adhesion between the perovskite phase and PEDOT:PSS, thus the perovskite phase cannot move on the PEDOT:PSS surface, and the grain growth near the contact interface is limited, leading to the formation of a small grain region.[43,44] In comparison, the perovskite phase can move on the surface of hydrophobic HTLs more easily, which is beneficial for larger grain formation. Therefore, the grains of the perovskite film fabricated on Triazine-Th-OMeTAD are much larger than those of the perovskite film on PEDOT:PSS.

We monitored the steady-state photoluminescence (PL) of the perovskite films fabricated on different concentrations of Triazine-Th-OMeTAD as well as PEDOT:PSS to investigate the charge extraction of different HTLs. The PL spectra show a wide absorption over the visible spectral range, with a PL peak at 780 nm, as shown in Fig. 4a. The PL intensities are obviously decreased in the samples with Triazine-Th-OMeTAD, compared to that with PEDOT:PSS, indicating that Triazine-Th-OMeTAD is more efficient to extract holes from the perovskite layer than PEDOT:PSS. The time-resolved photoluminescence (TRPL) was also performed to investigate the charge extraction and collection processes at the HTM/$MAPbI_3$ interface, as shown in Fig. 4b. The TRPL decay data were fitted with a multiexponential function (Table S1, ESI†).[45,46] The average carrier lifetimes of $MAPbI_3$ formed on PEDOT:PSS and various concentrations of Triazine-Th-OMeTAD (0.5 mg mL^{-1}, 1.0 mg mL^{-1}, 2.0 mg mL^{-1}, 3.0 mg mL^{-1} and 6.0 mg mL^{-1}) are 10.62, 6.78, 4.32, 4.11, 3.83 and 5.39 ns, respectively, implying that the charge carriers are

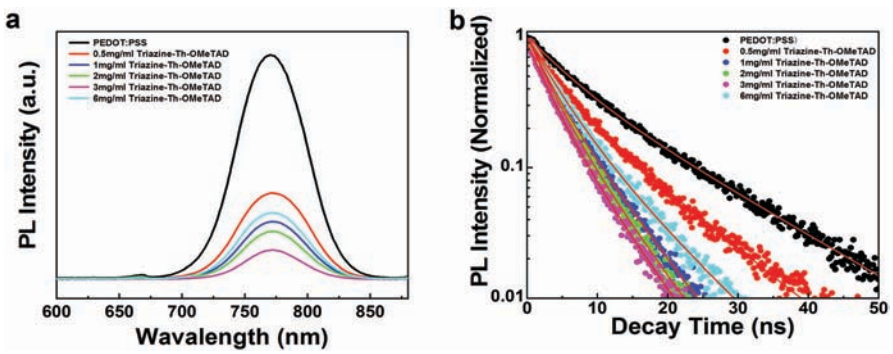

Fig. 4 (a) Steady-state PL spectra and (b) the decay curves of the TrPL intensity of the perovskite fabricated on the different concentrations of Triazine-Th-OMeTAD and PEDOT:PSS HTL using a 445 nm laser.

rapidly extracted from the perovskite at the perovskite/Triazine-Th-OMeTAD interface. X-Ray diffraction (XRD) characterization was employed to further survey the crystallinity of perovskite films based on Triazine-Th-OMeTAD and PEDOT:PSS. From the XRD results (Fig. S11, ESI†), the Triazine-Th-OMeTAD-based perovskites achieved significantly enhanced diffraction intensities of (110), (220) and (312) planes, compared with the PEDOT:PSS-based perovskites, suggesting the improvement in the crystallinity of the film. According to the TRPL and XRD results, it can be concluded that Triazine-Th-OMeTAD as the HTL is more conductive to the perovskite crystal growth and the extraction of charge carriers, compared with PEDOT:PSS. Moreover, the absorption of the perovskite film fabricated on 3 mg ml^{-1} Triazine-Th-OMeTAD is higher than that on PEDOT:PSS (Fig. S12, ESI†), which can be attributed to better film quality.

The trap density (n_{trap}) and hole mobility of the corresponding perovskite films are evaluated based on the space-charge-limited current (SCLC) measurements using the device structure of ITO/HTL/perovskite/Au in the dark.[40,45,47,48] Fig. 5 displays a kink in each dark *J–V* curve of six hole-only devices. When the applied voltage is lower than the kink-point voltage, the current density (J) increases linearly as V, indicating an Ohmic regime (n = 1). As it goes beyond the kink-point voltage, the current density (J) exhibits a sharp non-linear increase, indicating that the trap states are fully filled by the injected carriers, called a trap-filled limited regime ($n > 3$). Then, when the voltage further increases, there is a trap-free SCLC regime (n = 2). Here, trap density n_{trap} is linearly proportional to trap-filled limit voltage V_{TFL} at the kink point, which is a transition of *J–V* behavior from Ohmic to TFL:[49]

$$V_{TFL} = \frac{en_{trap}L^2}{2\varepsilon_0\varepsilon} \quad (1)$$

where L is the thickness of the perovskites, e is the electron charge, ε is the relative dielectric constant, and ε_0 is the vacuum permittivity. According to the SCLC analysis summarized in Table S2 (ESI†), the trap density of the perovskite based on 3.0 mg mL^{-1} Triazine-Th-OMeTAD is 1.73 × 10^{16} cm^{-3}, which is lower than that of the perovskite based on PEDOT:PSS (8.26 × 10^{16} cm^{-3}) or other concentrations of Triazine-Th-OMeTAD. We also calculated the hole mobility, μ_h, of each device by fitting the curves in the regime of trap-free SCLC. The μ_h of the perovskite fabricated on Triazine-Th-OMeTAD is higher than that fabricated on PEDOT:PSS (2.85 × 10^{-4} cm^2 V^{-1} s^{-1}), regardless of the concentrations except for 0.5 mg mL^{-1}, especially the device based on 3 mg mL^{-1} Triazine-Th-OMeTAD (1.73 × 10^{-3} cm^2 V^{-1} s^{-1}). All these results support that the Triazine-Th-OMeTAD hole transport material can reduce the trap density and carrier recombination in the perovskite films, resulting in higher sensitivity for photodetection. Concurrently, the high hole mobility and efficient charge extraction contribute to rapid response speed, which is consistent with the results of TRPL.

We also carried out the photocurrent measurements (under air mass 1.5 global illumination) of the OIHP photodetector with different concentrations of Triazine-Th-OMeTAD as HTLs, and compared to that of the PEDOT:PSS-based photodetector (Fig. S13, ESI†). We found that the photocurrents of the devices based on Triazine-Th-OMeTAD are higher than that of the device based on PEDOT:PSS, for all concentrations of Triazine-Th-OMeTAD. The photocurrent also increases with the increase of concentrations but decreases beyond a concentration of 3.0 mg mL^{-1}. The maximum photocurrent of 22.09 mA cm^{-2} is obtained with 3.0 mg mL^{-1} of Triazine-Th-OMeTAD. Therefore, we conclude that the Triazine-Th-OMeTAD as HTL not only increases the grains but also offers high photocurrent in the device. We further investigated the dark current of the devices based on PEDOT:PSS and different concentrations of Triazine-Th-OMeTAD, because the dark current is an important parameter to determine the performance

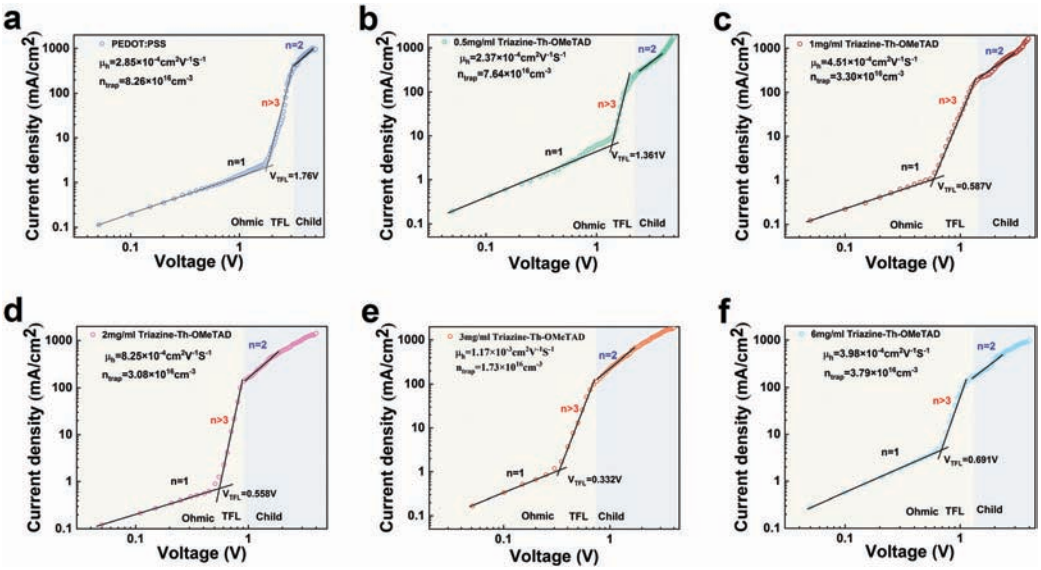

Fig. 5 Current density–voltage characteristics of the devices with ITO/HTL/perovskite/Au configuration, where HTL is (a) PEDOT:PSS; (b) 0.5 mg mL^{-1}; (c) 1.0 mg mL^{-1}; (d) 2.0 mg mL^{-1}; (e) 3.0 mg mL^{-1} and (f) 6.0 mg mL^{-1}, for estimating the defect density in the perovskite films.

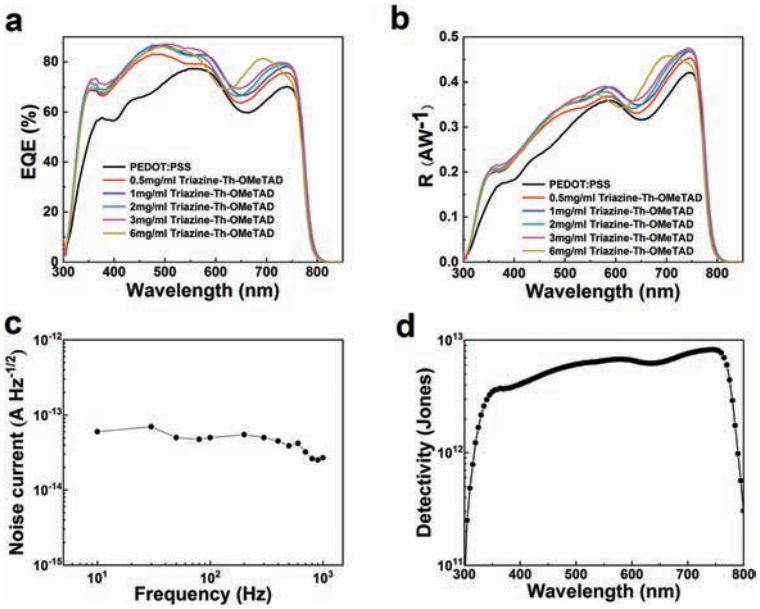

Fig. 6 (a) EQE and (b) spectral responsivity, *R*, of the devices with PEDOT:PSS and different concentrations of Triazine-Th-OMeTAD HTLs at zero bias; (c) noise current as a function of signal frequency; (d) the specific detectivity of the OIHP photodetector as a function of wavelength under zero bias.

of the photodetectors (Fig. S14, ESI†). The device based on 3.0 mg mL^{-1} Triazine-Th-OMeTAD exhibits the lowest dark current of 1.09 nA cm^{-2} at zero voltage. Fig. 6a shows the wavelength-dependent external quantum efficiency (EQE) measured at 210 Hz and zero bias. The device based on 3 mg mL^{-1} Triazine-Th-OMeTAD shows an EQE of ~80% in the visible region, and a peak value of 87% at 500 nm. The corresponding responsivity (*R*) curve is shown in Fig. 6b, indicating the maximum value of 0.47 A W^{-1} around 780 nm. From this, we can clearly see that, regardless of the concentration, the EQE and *R* of the Triazine-Th-OMeTAD-based devices are higher than those of the device based on PEDOT:PSS as HTL. This can be attributed to the (1) lower defect density and high-quality of the perovskite film fabricated on Triazine-Th-OMeTAD and (2) lesser charge recombination at the Triazine-Th-OMeTAD/$MAPbI_3$ interface than at the PEDOT:PSS/$MAPbI_3$ interface. In general, most of the photogenerated carriers are created near the $MAPbI_3$/HTL interface in the inverted structure devices due to the short penetration depth of high-energy photons and because the $MAPbI_3$/HTL interface is critical for charge recombination. The comprehensive studies of other characteristics of the optimized OIHP photodetector (based on 3.0 mg mL^{-1} of Triazine-Th-OMeTAD) are described below.

The measured noise current curve of the optimized OIHP photodetector is shown in Fig. 6c. The noise current is very low and is barely sensitive to frequency, indicating the successful passivation of the charge traps. The specific detectivity (D^*) is the most important parameter of device detection capability. Based on the measured noise and *R*, the D^* can be calculated according to the following equation:[8,50]

$$D^* = \frac{R\sqrt{AB}}{I_{noise}} \quad (2)$$

where *A* is the device working area and *B* is the bandwidth. The specific detectivity, D^*, of our optimized OIHP photodetectors as a function of spectral wavelength is presented in Fig. 6d. The specific D^* is above 4.0×10^{12} cm $Hz^{1/2}$ W^{-1} from 350 to 790 nm, with a peak value of 8.2×10^{12} cm $Hz^{1/2}$ W^{-1} at 780 nm, which is comparable with the commercial Si photodiode at the same wavelength. Therefore, with a suitable hole transporting material and interface engineering, the perovskite photodetector shows a great commercial potential. The linear dynamic range (LDR) of the OIHP photodetector is shown in Fig. 7a. The LDR is calculated by the following relation:[51,52]

$$\mathrm{LDR} = 20\log\frac{P_{sat}}{P_{low}} \quad (3)$$

where P_{sat} and P_{low} are the highest and the lowest light intensities among which the OIHP photodetector can keep the linear response to the light intensity. The highest light intensity of 4.3 mW cm^{-2} and the lowest light intensity of 2×10^{-8} mW cm^{-2} were achieved for our OIHP photodetector, corresponding to the LDR of 166 dB.

In addition to D^* and LDR, the response time is also an important parameter for photodetectors, because it determines the ability of photodetectors to truthfully record a high-frequency incident light signal. In our work, the transient photocurrent response (TPC) of the device under zero bias was measured by exciting with a nanosecond laser at a wavelength of 532 nm with a pulse width of around 1 ns and a repeating frequency of 20 Hz. The TPC signal was recorded using an oscilloscope with an input resistor of 50 Ω. As shown in Fig. 7b, the ultrafast response time of the Triazine-Th-OMeTAD-based photodetector is 18 ns for the rise time and 100 ns for the fall time with an active area of 11 mm^2. In contrast, the response time of the PEDOT:PSS-based device is 143 ns (Fig. S15, ESI†). To the best of our knowledge, the response time of 18 ns is the fastest response reported for OIHP

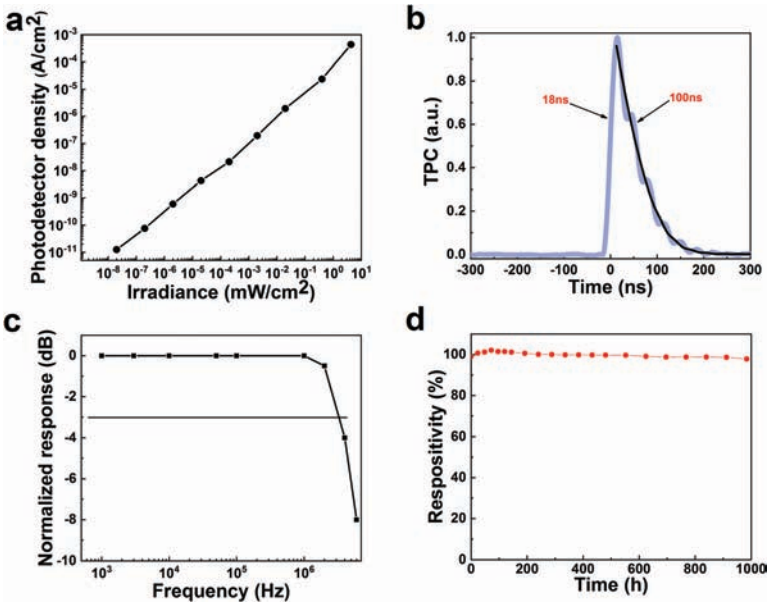

Fig. 7 (a) Linear dynamic range of the OIHP photodetector under a laser illumination of various light intensities; (b) transient photocurrent response of the Triazine-Th-OMeTAD-based OIHP photodetector with a device area of 11 mm^2 in the photovoltaic mode; (c) normalized frequency response of the Triazine-Th-OMeTAD-based OIHP photodetector, the line of −3 dB is depicted for reference; (d) variation in the spectral responsivity of the OIHP photodetector without encapsulation over a storage time of 1000 h in air (RH 20–30%).

photodetectors compared with the previous reports shown in Table 2.[9,14,17,23,53–55] The rise time was defined as the time for the current to rise from 10% to 90% of the maximum value while the fall time was defined as the response decreasing from 90% to 10% of the maximum value. Such a fast response speed is attributed to the minimal trap charge recombination inside the perovskite film as well as at the interface, and the efficient charge extraction due to high mobility and suitable energy level of the hole transporting material. In addition, the time-dependent current (I–t) curve of the device is measured with a bias voltage of 0 V (self-power condition) and bias 0.1 V under monochromatic light (Fig. S16, ESI†). Under continuous testing conditions, the photodetector exhibits stable and reproducible photocurrent for several cycles, which meets the requirement for real application.

The photocurrent response as a function of the modulation frequency of the incident light is shown in Fig. 7c. The OIHP photodetectors with an active area of 11 mm^2 achieved a 3 dB cut-off frequency of 3 MHz. This result provides direct evidence of the excellent performance in optical communication for our OIHP photodetectors. Long-term stability is another key parameter for the practical applications of photodetectors, which is still a challenging issue for many devices. To study the long-term stability of self-powered photodetectors based on Triazine-Th-OMeTAD, the spectral responsivity of the device was measured periodically at a bias voltage of 0 V under 675 nm illumination. The device was stored in air at room temperature with a relative humidity (RH) of 20–30% without any encapsulation. As shown in Fig. 7d, the device provided excellent stability over 1000 h with only a slight reduction in responsivity, and still maintained at more than 98% of the initial value, showing long-term stability. The excellent long-term stability of our devices can be ascribed to the hydrophobic nature of Triazine-Th-OMeTAD, which has better stability than the hydrophobic PEDOT:PSS.

Conclusions

In summary, we fabricated solution-processed OIHP photodetectors with dopant-free HTLs and demonstrated their excellent performance characteristics. The star-shaped Triazine-Th-OMeTAD favors the subsequent formation of

Table 2 Comparison of critical parameters of OIHP photodetectors

Material	Area (mm^2)	Wavelength (nm)	D^* (Jones)	Rising time (ns)	Ref.
PTAA/$MAPbI_3$/C_{60}	0.04	300–780	7.8×10^{12} (700 nm)	0.95	9
PTAA/$MAPbI_3$SC/C_{60}	0.6	300–780	1.5×10^{13} (700 nm)	295	54
PTAA/$MAPbI_3$/IEICO/C_{60}	0.6	300–900	7.37×10^{11} (820 nm)	27	55
PEDOT:PSS/$MaPbI_{3-x}Cl_x$/PCBM	1	300–780	3.11×10^{11} (550 nm)	180	23
m-MTDATA:F4-TCNQ/$MAPbI_3$/C_{60}	4.4	300–780	1×10^{12} (750 nm)	39.8	17
NiOx:PbI_2/$MAPbI_3$/C_{60}	6	300–780	10^{13} (750 nm)	168	53
OTPD/$MAPbI_3$/PCBM/C_{60}	7.25	300–780	7.4×10^{12} (680 nm)	120	14
Triazine-Th-OMeTAD//$MAPbI_3$/PCBM	11	300–780	8.2×10^{12} (700 nm)	18	This work

high-quality crystalline $MAPbI_3$ films and passivates the surface of the perovskite. Moreover, the Triazine-Th-OMeTAD layer offers a large electron injection barrier at the ITO interface for suppressing dark current and the favorable energy-level alignment with the perovskite film for enhancing the hole extraction. Upon optimization of the thickness (concentrations) of the Triazine-Th-OMeTAD, an ultralow dark current density of 1.09×10^{-9} A cm^{-2} at zero bias was achieved. Besides, a large specific detectivity above 10^{12} Jones, a high LDR of 166 dB, and an ultrafast response time of 18 ns are achieved with a large active area of 11 mm^2. We believe that this ultrafast-response OIHP photodetector will find application in consumer electronics, due to the suitable optical absorption spectrum for visible imaging, fast response speed for quick frame rate imagers and high cut-off frequency for optical communication.

Experimental section

Fabrication of $MAPbI_3$ perovskite films

To prepare perovskite precursors, 1.0 M PbI_2 (99.99%, TCI) and 1.0 M MAI (Aus) were dissolved in 1 mL of a mixed polar solvent of dimethylformamide and dimethyl sulfoxide at a volume ratio of 4 : 1. Then, the mixture was stirred at 60 °C for about 4 h. After that, this solution was filtered by 0.22 μm syringe PTFE filters. The $MAPbI_3$ perovskite precursor was spin-coated on the ITO/Triazine-Th-OMeTAD or PEDOT:PSS substrates at a rate of 4000 rpm for 25 s, and 130 μL of anisole as the anti-solvent was mildly dripped on the spinning substrates in the fourth second. The spin-coated thin films were annealed at 100 °C for 10 min for converting the precursors to perovskite films. It should be noted that all the processes were conducted in a nitrogen-filled glove box.

Device fabrication

The device architecture of the perovskite photodetector is ITO/HTL/$MAPbI_3$/$PC_{61}BM$/BCP/Ag. The ITO glass substrates (Advanced Election Technology Co. Ltd) were cleaned with a Hellmanex™ cleaning solution (diluted with water in 2 : 98 v : v ratio), deionized water, acetone, and ethanol in an ultrasonic bath for 15 min. After that, the ITO glasses were treated in a UV cleaner for 20 min. Different concentrations (0.5, 1, 2, 3, 6 mg mL^{-1}) of Triazine-Th-OMeTAD were dissolved in chlorobenzene in advance, then spin-coated onto the ultraviolet-ozone-treated ITO substrates at 5000 rpm for 45 s and annealed at 150 °C for 10 min under ambient conditions. For comparison, PEDOT:PSS was spin-coated on some ITO glasses and annealed at 150 °C for 10 min under ambient conditions. Then, the prepared samples were transferred to a nitrogen-filled glove box. The $MAPbI_3$ perovskite films were deposited on the prepared substrates. Subsequently, 20 mg mL^{-1} $PC_{61}BM$ (99.5%, Nano-C) in chlorobenzene was spin-coated on the perovskite films at 2000 rpm for 30 s, followed by spin-coating 0.5 mg mL^{-1} bathocuproine (98%$^+$, Adamas) in ethanol at 4000 rpm for 40 s. Finally, 100 nm silver was deposited on the top through thermal evaporation under a vacuum of 10^{-4} Pa as the cathode. The active area of the perovskite photodetectors was 11 mm^2.

Film characterization

The top-view morphology images of the $MAPbI_3$ perovskites were characterized using a Zeiss Merlin scanning electron microscope (SEM). The time-resolved PL measurements were performed with an Edinburgh FS-5 spectrometer equipped with an excitation source of a 450 nm pulsed laser. The UV-vis absorption spectra were recorded on a PERSEE TU1901 spectrophotometer. The XRD patterns were collected using a Rigaku SmartLab 9 kW system with Cu-Kα radiation. The surface roughness and film thickness were measured using an Asylum Research MFP-3D-Stand Alone atomic force microscope.

Device characterization

The dark current density against voltage was recorded using a Keithley 4200 parameter analyzer. The photocurrent density–voltage (*J–V*) characteristics of PSCs were measured using a Keithley 2400 parameter analyzer under 1 sun solar spectrum illumination (AM 1.5 G) with an intensity of 100 mW cm^2 calibrated *via* a silicon reference cell. The EQE measurements were conducted under short-circuit conditions through a lock-in amplifier under illumination with monochromatic light from a xenon arc lamp. The linear dynamic range measurements were performed under different intensities of monochromatic light using Thorlabs metallic-coated neutral density filters. The intensity of the monochromatic light was measured by facility-calibrated (Newport) Si photodetectors. The noise current of the photodetectors was measured employing a Stanford Research SR830 lock-in-amplifier in the current measurement mode. The transient photocurrent response was measured with a 532 nm, 1 ns pulse width laser integrated with an optical chopper and a 350 MHz Tektronix MDO3034 oscilloscope. The frequency response was recorded with a 520 nm LED driven by a Tektronix AGF1062A function generator and a digital storage oscilloscope.

Author contributions

G. Q. L. and A. K. K. Kyaw conceived and directed the research. C. W. S. designed the experiments, fabricated the devices, and acquired the data. F. M. synthesized the hole transporting materials. Z. X. W. and H. B. M. carried out the DFT calculations for energy formation. J. H. Y., W. H. L., D. Y. F., and R. C. performed material characterizations. C. W. S. wrote the manuscript. All of the authors contributed to the discussions.

Conflicts of interest

The authors declare no conflict of interest.

Acknowledgements

Prof. A. K. K. Kyaw thanks the general support by the Guangdong Basic and Applied Basic Research Foundation (2020A1515010916), the Guangdong University Key Laboratory for Advanced Quantum Dot Displays and Lighting (No. 2017KSYS007), and the High-level University Fund (G02236004).

Prof. G. Li thanks the general support by the National Key R&D Program of China (2017YFA0204704), the National Science Foundation of China (51773091, 22075140, 61604069), the Nature Science Foundation of Jiangsu Province (BK20171465) and the Open Project Program of Wuhan National Laboratory for Optoelectronics (No. 2020WNLOKF010).

Notes and references

1 M. Law, H. Kind, B. Messer, F. Kim and P. D. Yang, *Angew. Chem., Int. Ed.*, 2002, **41**, 2405–2408.
2 X. H. Gao, Y. Y. Cui, R. M. Levenson, L. W. K. Chung and S. M. Nie, *Nat. Biotechnol.*, 2004, **22**, 969–976.
3 T. Y. Zhai, X. S. Fang, M. Y. Liao, X. J. Xu, L. Li, B. D. Liu, Y. Koide, Y. Ma, J. N. Yao, Y. Bando and D. Golberg, *ACS Nano*, 2010, **4**, 1596–1602.
4 L. Su, Z. X. Zhao, H. Y. Li, J. Yuan, Z. L. Wang, G. Z. Cao and G. Zhu, *ACS Nano*, 2015, **9**, 11310–11316.
5 J. Huang, Y. Yuan, Y. Shao and Y. Yan, *Nat. Rev. Mater.*, 2017, **2**, 17042.
6 G. C. Xing, N. Mathews, S. S. Lim, N. Yantara, X. F. Liu, D. Sabba, M. Gratzel, S. Mhaisalkar and T. C. Sum, *Nat. Mater.*, 2014, **13**, 476–480.
7 Y. P. He and G. Galli, *Chem. Mater.*, 2014, **26**, 5394–5400.
8 Y. L. Xu and Q. Q. Lin, *Appl. Phys. Rev.*, 2020, **7**, 011315.
9 L. Shen, Y. J. Fang, D. Wang, Y. Bai, Y. H. Deng, M. M. Wang, Y. F. Lu and J. S. Huang, *Adv. Mater.*, 2016, **28**, 10794–10800.
10 H. L. Zhu, Z. F. Liang, Z. B. Huo, W. K. Ng, J. Mao, K. S. Wong, W. J. Yin and W. C. H. Choy, *Adv. Funct. Mater.*, 2018, **28**, 1706068.
11 H. L. Loi, J. P. Cao, X. Y. Guo, C. K. Liu, N. X. Wang, J. J. Song, G. Q. Tang, Y. Zhu and F. Yan, *Adv. Sci.*, 2020, **7**, 2000776.
12 Z. L. Chen, C. L. Li, A. A. Zhumekenov, X. P. Zheng, C. Yang, H. Z. Yang, Y. He, B. Turedi, O. F. Mohammed, L. Shen and O. M. Bakr, *Adv. Opt. Mater.*, 2019, **7**, 1900506.
13 B. R. Sutherland, A. K. Johnston, A. H. Ip, J. X. Xu, V. Adinolfi, P. Kanjanaboos and E. H. Sargent, *ACS Photonics*, 2015, **2**, 1117–1123.
14 Y. J. Fang and J. S. Huang, *Adv. Mater.*, 2015, **27**, 2804–2810.
15 C. Liu, K. Wang, C. Yi, X. J. Shi, P. C. Du, A. W. Smith, A. Karim and X. Gong, *J. Mater. Chem. C*, 2015, **3**, 6600–6606.
16 R. Dong, Y. J. Fang, J. Chae, J. Dai, Z. G. Xiao, Q. F. Dong, Y. B. Yuan, A. Centrone, X. C. Zeng and J. S. Huang, *Adv. Mater.*, 2015, **27**, 1912–1918.
17 D. Z. Zhang, C. Y. Liu, Z. Q. Li, X. Y. Zhang, X. L. Zhang, S. P. Ruan, X. D. Zhang and W. B. Guo, *J. Mater. Chem. A*, 2018, **6**, 21039–21046.
18 R. Q. Guo, F. Huang, K. B. Zheng, T. Pullerits and J. J. Tian, *ACS Appl. Mater. Interfaces*, 2018, **10**, 35656–35663.
19 H. D. Pham, Z. F. Wu, L. K. Ono, S. Manzhos, K. Feron, N. Motta, Y. B. Qi and P. Sonar, *Adv. Electron. Mater.*, 2017, **3**, 1700139.
20 H. D. Pham, T. T. Do, J. Kim, C. Charbonneau, S. Manzhos, K. Feron, W. C. Tsoi, J. R. Durrant, S. M. Jain and P. Sonar, *Adv. Energy Mater.*, 2018, **8**, 13170300.
21 Q. Xiao, F. Wu, M. M. Han, Z. Li, L. N. Zhu and Z. A. Li, *J. Mater. Chem. A*, 2018, **6**, 13644–13651.
22 H. D. Pham, X. Q. Li, W. H. Li, S. Manzhos, A. K. K. Kyaw and P. Sonar, *Energy Environ. Sci.*, 2019, **12**, 1177–1209.
23 L. T. Dou, Y. Yang, J. B. You, Z. R. Hong, W. H. Chang, G. Li and Y. Yang, *Nat. Commun.*, 2014, **5**, 5404.
24 C. Bi, Q. Wang, Y. C. Shao, Y. B. Yuan, Z. G. Xiao and J. S. Huang, *Nat. Commun.*, 2015, **6**, 7747.
25 X. Lai, F. Meng, Q. Q. Zhang, K. Wang, G. Q. Li, Y. P. Wen, H. B. Ma, W. H. Li, X. Q. Li, A. K. K. Kyaw, K. Wang, X. W. Sun, M. Z. Du, X. Guo, J. P. Wang and W. Huang, *Sol. RRL*, 2019, **3**, 1900011.
26 X. Lai, M. Z. Du, F. Meng, G. Q. Li, W. H. Li, A. K. K. Kyaw, Y. P. Wen, C. G. Liu, H. B. Ma, R. Zhang, D. Y. Fan, X. Guo, Y. H. Wang, H. R. Ji, K. Wang, X. W. Sun, J. P. Wang and W. Huang, *Small*, 2019, **15**, 1904715.
27 F. Meng, Y. Wang, Y. Wen, X. Lai, W. Li, A. K. K. Kyaw, R. Zhang, D. Fan, Y. Li, M. Du, X. Guo, H. Ma, G. Li, X. W. Sun and J. Wang, *Sol. RRL*, 2020, 2000327.
28 K. Rakstys, S. Paek, P. Gao, P. Gratia, T. Marszalek, G. Grancini, K. T. Cho, K. Genevicius, V. Jankauskas, W. Pisula and M. K. Nazeeruddin, *J. Mater. Chem. A*, 2017, **5**, 7811–7815.
29 B. Chen, P. N. Rudd, S. Yang, Y. B. Yuan and J. S. Huang, *Chem. Soc. Rev.*, 2019, **48**, 3842–3867.
30 G. W. T. M. J. Frisch, H. B. Schlegel, G. E. Scuseria, M. A. Robb, J. R. Cheeseman, G. Scalmani, V. Barone, B. Mennucci, G. A. Petersson, H. Nakatsuji, M. Caricato, X. Li, H. P. Hratchian, A. F. Izmaylov, J. Bloino, G. Zheng, J. L. Sonnenberg, M. Hada, M. Ehara, K. Toyota, R. Fukuda, J. Hasegawa, M. Ishida, T. Nakajima, Y. Honda, O. Kitao, H. Nakai, T. Vreven, J. A. Montgomery, Jr., J. E. Peralta, F. Ogliaro, M. Bearpark, J. J. Heyd, E. Brothers, K. N. Kudin, V. N. Staroverov, R. Kobayashi, J. Normand, K. Raghavachari, A. Rendell, J. C. Burant, S. S. Iyengar, J. Tomasi, M. Cossi, N. Rega, J. M. Millam, M. Klene, J. E. Knox, J. B. Cross, V. Bakken, C. Adamo, J. Jaramillo, R. Gomperts, R. E. Stratmann, O. Yazyev, A. J. Austin, R. Cammi, C. Pomelli, J. W. Ochterski, R. L. Martin, K. Morokuma, V. G. Zakrzewski, G. A. Voth, P. Salvador, J. J. Dannenberg, S. Dapprich, A. D. Daniels, Ö. Farkas, J. B. Foresman, J. V. Ortiz, J. Cioslowski and D. J. Fox, *Gaussian 09*, Gaussian, Inc., Wallingford CT, 2009.
31 X. H. Zhang and R. F. Jin, *Front. Chem.*, 2019, **7**, 122.
32 G. Zhang and C. B. Musgrave, *J. Phys. Chem. A*, 2007, **111**, 1554–1561.
33 J. Ku, Y. Lansac and Y. H. Jang, *J. Phys. Chem. C*, 2011, **115**, 21508–21516.
34 L. H. Zhang, K. Pei, M. D. Yu, Y. L. Huang, H. B. Zhao, M. Zeng, Y. Wang and J. W. Gao, *J. Phys. Chem. C*, 2012, **116**, 26154–26161.
35 P. Qi, F. Zhang, X. M. Zhao, X. C. Liu, X. D. Bi, P. Wei, Y. Xiao, X. G. Li and S. R. Wang, *Energy Technol.*, 2017, **5**, 1173–1178.
36 F. Z. X. M. Zhao, C. Y. Yi, D. Q. Bi, X. D. Bi, P. Wei, J. S. Luo, X. C. Liu, S. R. Wang, X. G. Li, S. M. Zakeeruddin and M. Grätzel, *J. Mater. Chem. A*, 2016, **4**, 16330.

37 K. Rakstys, M. Saliba, P. Gao, P. Gratia, E. Kamarauskas, S. Paek, V. Jankauskas and M. K. Nazeeruddin, *Angew. Chem., Int. Ed.*, 2016, **55**, 7464–7468.
38 T. S. Qin, W. C. Huang, J. E. Kim, D. J. Vak, C. Forsyth, C. R. McNeill and Y. B. Cheng, *Nano Energy*, 2017, **31**, 210–217.
39 C. H. M. Chuang, P. R. Brown, V. Bulovic and M. G. Bawendi, *Nat. Mater.*, 2014, **13**, 796–801.
40 Y. Zhao, C. L. Li, J. Z. Jiang, B. M. Wang and L. Shen, *Small*, 2020, **16**, 2001534.
41 W. Jang, S. Rasool, B. G. Kim, J. Kim, J. Yoon, S. Manzhos, H. K. Lee, I. Jeon and D. H. Wang, *Adv. Funct. Mater.*, 2020, **30**, 2001402.
42 B. G. Kim, W. Jang, S. Seo, A. Shawky, M. S. Kim, K. Kim, B. Mikladal, E. I. Kauppinen, S. Maruama, Il Jeon and D. H. Wang, *Nano Today*, 2021, **37**, 101081.
43 X. P. Zheng, B. Chen, J. Dai, Y. J. Fang, Y. Bai, Y. Z. Lin, H. T. Wei, X. C. Zeng and J. S. Huang, *Nat. Energy*, 2017, **2**, 17102.
44 S. Xiao, Y. Bai, X. Y. Meng, T. Zhang, H. N. Chen, X. L. Zheng, C. Hu, Y. Q. Qu and S. H. Yang, *Adv. Funct. Mater.*, 2017, **27**, 1604944.
45 W. H. Li, X. Lai, F. Meng, G. Q. Li, K. Wang, A. K. K. Kyaw and X. W. Sun, *Sol. Energy Mater. Sol. Cells*, 2020, **211**, 110527.
46 Q. Jiang, Y. Zhao, X. W. Zhang, X. L. Yang, Y. Chen, Z. M. Chu, Q. F. Ye, X. X. Li, Z. G. Yin and J. B. You, *Nat. Photonics*, 2019, **13**, 460–466.
47 D. Y. Son, S. G. Kim, J. Y. Seo, S. H. Lee, H. Shin, D. Lee and N. G. Park, *J. Am. Chem. Soc.*, 2018, **140**, 1358–1364.
48 H. W. Zhu, F. Zhang, Y. Xiao, S. R. Wang and X. G. Li, *J. Mater. Chem. A*, 2018, **6**, 4971–4980.
49 H. R. Tan, A. Jain, O. Voznyy, X. Z. Lan, F. P. G. de Arquer, J. Z. Fan, R. Quintero-Bermudez, M. J. Yuan, B. Zhang, Y. C. Zhao, F. J. Fan, P. C. Li, L. N. Quan, Y. B. Zhao, Z. H. Lu, Z. Y. Yang, S. Hoogland and E. H. Sargent, *Science*, 2017, **355**, 722–726.
50 Y. H. Dong, Y. S. Zou, J. Z. Song, X. F. Song and H. B. Zeng, *J. Mater. Chem. C*, 2017, **5**, 11369–11394.
51 W. B. Wang, D. W. Zhao, F. J. Zhang, L. D. Li, M. D. Du, C. L. Wang, Y. Yu, Q. Q. Huang, M. Zhang, L. L. Li, J. L. Miao, Z. Lou, G. Z. Shen, Y. Fang and Y. F. Yan, *Adv. Funct. Mater.*, 2017, **27**, 1703953.
52 R. D. Jansen-van Vuuren, A. Armin, A. K. Pandey, P. L. Burn and P. Meredith, *Adv. Mater.*, 2016, **28**, 4766–4802.
53 H. L. Zhu, J. Q. Cheng, D. Zhang, C. J. Liang, C. J. Reckmeier, H. Huang, A. L. Rogach and W. C. H. Choy, *ACS Nano*, 2016, **10**, 6808–6815.
54 C. X. Bao, Z. L. Chen, Y. J. Fang, H. T. Wei, Y. H. Deng, X. Xiao, L. L. Li and J. S. Huang, *Adv. Mater.*, 2017, **29**, 1703209.
55 C. L. Li, J. R. Lu, Y. Zhao, L. Y. Sun, G. X. Wang, Y. Ma, S. M. Zhang, J. R. Zhou, L. Shen and W. Huang, *Small*, 2019, **15**, 1903599.

